ARCHIVES OF ELECTRICAL ENGINEERING VOL. 71(4), pp. 865–880 (2022)

DOI 10.24425/aee.2022.142113

Comparison of concentrated winding topologies considering transient voltages in the winding system of inverter-driven low-voltage machines

FLORIAN PAULI, NIKLAS DRIENDL ✉, SEBASTIAN MÖNNINGHOFF, KAY HAMEYER

Institute of Electrical Machines (IEM), RWTH Aachen University
Germany

e-mail: niklas.driendl@iem.rwth-aachen.de

(Received: 20.06.2022, revised: 27.06.2022)

Abstract: To reduce the losses of the power electronic inverter, the voltage slew rate (du/dt) of the electric motors supplying voltage is increasing. As steep voltage slopes excite high frequencies in the megahertz range, transient phenomena in the winding of the electrical machine occur. To design the insulation system, the maximum electric potential difference between the conducting elements must be predicted. General design rules can lead to a significant overengineering of the interturn insulation, particularly when considering smaller stators with a known wire distribution. Therefore, two different winding topologies are studied comparing the voltage distribution in a round-wire winding and a winding with preformed coils.

Key words: du/dt, electrical machines, insulation system, inverters, transient voltages

1. Introduction

This article is dedicated to Professor Andrzej Demenko and Professor Lech Nowak in recognition of their lifetime contribution to the field of Electric Machines.

Transient voltages in the windings of electrical machines occur due to switching processes of the semiconductors of the power electronic inverter. Caused by the steep voltage slope, they can lead to a high voltage drop between various conducting components of the winding system. Therefore, a high electric field strength occurs inside the insulation system increasing the risk of partial discharges. These discharges damage the insulation material and can lead to a breakdown of the insulation system within minutes to hours. Low-voltage electrical machines are usually

designed to be partial discharge-free during the entire lifetime. Therefore, the voltage between two conducting parts has to be lower than the partial discharge inception voltage at each operation point. The occurrence of transients in grid-connected machines is well known for decades [1, 2]. These transients are caused by switching processes and events of failure in the grid. Contrary to this, the switching process in inverter driven machines occurs periodically. With the rising popularity of such drives in the 1990's, several publications on the mapping of the voltage distribution in larger machines occurred [3]. Presently, the voltage slew rate ($\mathrm{d}u/\mathrm{d}t$) of drive systems is increasing, as a short switching progress mitigates the switching losses in the power electronic circuit. Silicon Carbide (SiC)-based inverters reach voltage rise times in the range as low as 20 ns and voltage slew rates of up to 50 kV/µs. Gallium Nitride (GaN)-based systems can reach rise times in the range of 4 ns and slew rates of > 200 kV/µs [4]. This trend of faster switching processes however leads to the occurrence of faster transients with shorter wavelength inside the windings of inverter-driven electrical machines. As a consequence, the impact of transient voltages on the insulation system becomes more severe. Design criteria for the insulation systems from the standards such as IEC 60034-18-41 [5] only consider significantly longer voltage rise times of more than 0.1 µs. Therefore, current research focuses on enhancing detailed modelling of the voltage distribution in the winding systems [6–9] and on modelling partial discharge processes, which result from excessively high voltage peeks as well as on the resulting electric aging process [10–13].

The aim of this paper is to compare the influence of transient voltages on the interturn insulation of machines with different winding topologies. For this purpose, two electric wheel hub traction motors, which are identical apart from their windings, are studied. One machine – in the following denoted as machine A – is equipped with a conventional round-wire winding while the other one (machine B) is equipped with a preformed coil. Further details on the setup and on the production process of the two machines are given in [14–16].

2. Winding topologies

Both machines, which are considered in this paper, are equipped with concentrated windings. Machine A is constructed with 100 conductors per coil, while, due to the feasibility of the production process, there are only 20 conductors per coil in machine B (cp. Fig. 1). To achieve similar operational properties of both machines, in machine A all 20 coils per strand are connected in parallel, while there are four sets of series connected coils in machine B (cp. Fig. 2). An unwound coil of machine A reaches a length of 18 m, while an unwound coil of machine B is only 3.6 m long. Due to the configuration of the winding, however, the distance between the machine terminals and the star point is 18 m for both topologies.

The basic data of the two winding systems is summarized in Table 1:

When studying transient voltage phenomena, considering the size of the regarded object is crucial. The velocity of the voltage propagation c is limited. In the analogue of a lossless coaxial cable, c can be calculated as:

$$c = \frac{c_0}{\sqrt{\varepsilon_\mathrm{r} \cdot \mu_\mathrm{r}}}, \tag{1}$$

where: c_0 is the vacuum speed of light, ε_r is the relative permittivity of the dielectric material and μ_r is the relative permeability. Transient phenomena in a conductor of the length l become relevant as the wave length λ of the voltage component with the maximum considered frequency f_{max} is

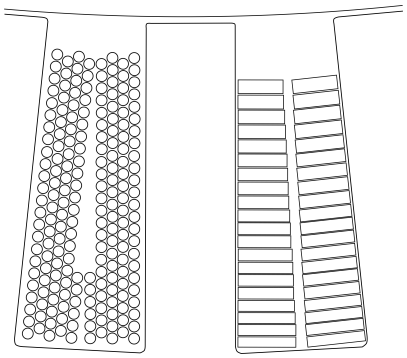

Fig. 1. Slot geometry of machine A (left) and machine B (right) [16]

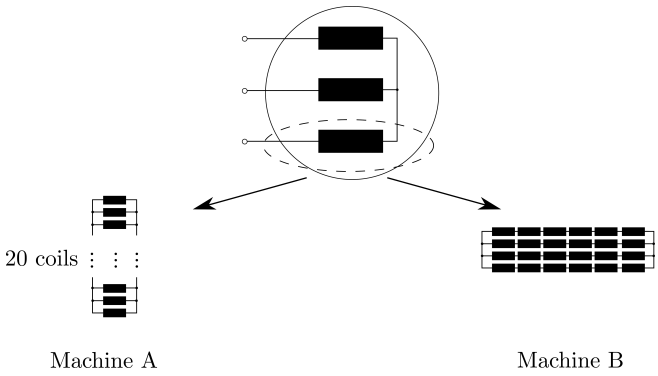

Fig. 2. Topology of series and parallel connected coils in machines A and B

Table 1. Winding paramters of both studied machines

Quantity	**Machine A**	**Machine B**
Number of strands m	3	
Polepair number p	20	
Fractional slot q	0.5	
Number of turns (per coil) n	100	20
Number of parallel connected coils	20	4
Length of the winding in one coil l_{coil}	18 m	3.6 m
Length of winding from terminal to star point l_{phase}	18 m	

no longer significantly larger than the conductor itself. As a rule of thumb, the threshold is often considered being [17]:

$$\frac{\lambda}{l} = \frac{c}{l \cdot f_{\max}} > 60. \tag{2}$$

The estimation of the voltage propagation speed by considering a lossless transmission line only holds roughly. Regarding the ferromagnetic stator as the return conductor introduces a highly nonlinear material behaviour. The contribution of the relative permeability μ_r depends on the frequency dependent penetration depth of the iron core and the general slot geometry. Also, the relative permittivity is frequency dependent and therefore introduces another challenge when regarding non-sinusoidal voltage waveforms. As most insulation materials have a relative permittivity of $\varepsilon_r \approx 4$ and lossy materials as well as a permeability of $\mu_r > 1$, the decrease in propagation velocity, in this paper, is assumed to be:

$$c \lesssim \frac{c_0}{2}. \tag{3}$$

Nowadays, SiC-inverter reach voltage risetimes of less than $t_r = 20$ ns. According to [17], a voltage slope mainly excites a frequency of

$$f = \frac{1}{4t_r}. \tag{4}$$

For the given voltage step, this refers to a frequency of $\boldsymbol{f = 125\ \mathrm{MHz}}$ and therefore to a wavelength of $\boldsymbol{\lambda = 12\ \mathrm{m}}$ for a propagation velocity of $\boldsymbol{c = 150\ \mathrm{m/\mu s}}$. Consequently, transient voltages must be considered in the given machine with reference to Eq. (2).

3. Effects of transients on the turn-to-turn voltage

In this paper, the voltage drop between two adjacent turns is focused. In Fig. 3, the turns are numbered according to the current path of the winding. For machine A, the largest expected voltage drop over the interturn occurs between turns 1 and turn 47, while for machine B it occurs between turns 1 and 2.

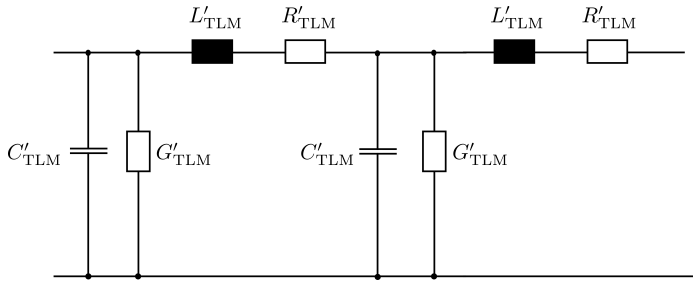

Fig. 3. Two equivalent circuit elements of a transmission line

An analytically well understood setup for the consideration of high frequency effects is a lossy, but dispersion free coaxial cable. Such a cable can be modelled as a series connection of multiple

equivalent circuit elements, as displayed in Fig. 3. A coil, however, consists of several turns which results in a capacitive coupling. Therefore, high frequency electromagnetic waves can be conducted along different paths: along the conductors and from turn to turn via capacitive or inductive coupling. Both paths are displayed in Fig. 4. The path along the conductor is longer and has lowpass characteristics while the path from turn to turn primarily functions as a high pass.

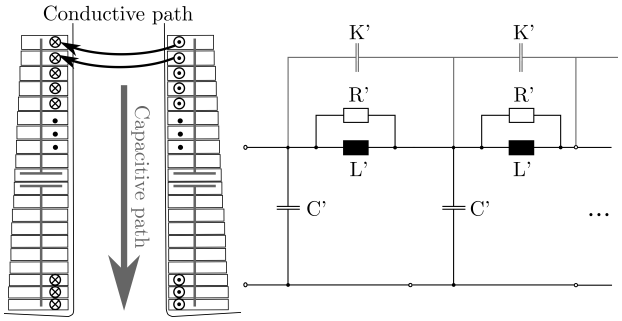

Fig. 4. Capacitive and inductive path through the machine (left) and a corresponding equivalent circuit diagram (right)

The winding can be modelled by an infinite chain of equivalent circuits (cp. Fig. 4). The electric behaviour of the model is given by a differential equation [18]:

$$\frac{1}{R'}\frac{\partial^3 u(x,t)}{\partial x^2 \partial t} + K'\frac{\partial^4 u(x,t)}{\partial x^2 \partial t^2} + \frac{1}{L'}\frac{\partial^2 u(x,t)}{\partial x^2} = \frac{C'\partial^2 u(x,t)}{\partial t^2}\,, \tag{5}$$

where R', K', C' and L' are the line parameters per unit length according to Fig. 4 and u is the voltage at location x and time t.

The parallel placement of the resistor R' and the inductor L' already allows for the consideration of increased losses at higher frequencies due to eddy current losses. However, due to the pronounced non-linearity of this effect, the first order L-R-element cannot accurately express the winding's behaviour over a large frequency range. Due to non-linearities and frequency dependencies of the insulation material behaviour also the capacitances cannot be assumed as constant. Therefore, the accuracy of Eq. (5) is limited. The strongly frequency dependent behaviour of the inductance and the resistance can be modelled by replacing the elements L' and R' by a so-called L-R-ladder, as presented in [4]. However, this approach results in a huge parametrization effort. Therefore, in this work, high- and low-frequency behaviour of the winding is regarded separately by considering the conductive and the capacitive path, respectively.

When a voltage step is applied to the stator and is propagating along the conductive path, two processes must be considered (cp. Fig. 5):

- Due to the finite velocity of the voltage, there is an increasing time delay from turn to turn. In Fig. 5, this delay is marked by t_{db}.
- Due to eddy currents, the effective resistance of the winding is severely larger for high frequencies than for low frequencies. Thus, higher frequencies are relatively more damped and the voltage risetime decreases.

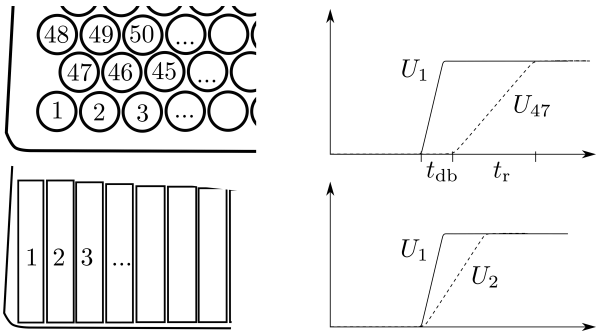

Fig. 5. Neighbouring turns in machines A and B and influence of the position on the voltage step. Inevitable *overshoot* and *ringing* are not displayed

Both effects can result in a large voltage drop across the interturn insulation of adjacent turns, particularly, when the distance along the winding, between neighbouring turns, is large.

When only one frequency component is considered, the complex voltage U at the location x in the transmission line model (cp. Fig. 3) can be described as

$$\underline{U}(x) = \underline{U}(x = 0) \cdot \exp(x\underline{\gamma}), \tag{6}$$

where $\underline{\gamma}$ is the complex propagation constant:

$$\underline{\gamma} = \alpha + \mathrm{j}\beta = \sqrt{(R'_{\mathrm{TLM}} + \mathrm{j}\omega L'_{\mathrm{TLM}})(G'_{\mathrm{TLM}} + \mathrm{j}\omega C'_{\mathrm{TLM}})}\,, \tag{7}$$

where the real part of the propagation constant α describes the damping and the imaginary part β describes the phase shift:

$$\alpha = \sqrt{\begin{array}{l}\dfrac{1}{2}\sqrt{\left(R'^2_{\mathrm{TLM}} + \omega^2 L'^2_{\mathrm{TLM}}\right)\left(G'^2_{\mathrm{TLM}} + \omega^2 C'^2_{\mathrm{TLM}}\right)} \\ \quad + \dfrac{1}{2}\left(R'_{\mathrm{TLM}} G'_{\mathrm{TLM}} - \omega^2 L'_{\mathrm{TLM}} C'_{\mathrm{TLM}}\right)\end{array}}\,, \tag{8}$$

$$\beta = \sqrt{\begin{array}{l}\dfrac{1}{2}\sqrt{\left(R'^2_{\mathrm{TLM}} + \omega^2 L'^2_{\mathrm{TLM}}\right)\left(G'^2_{\mathrm{TLM}} + \omega^2 C'^2_{\mathrm{TLM}}\right)} \\ \quad - \dfrac{1}{2}\left(R'_{\mathrm{TLM}} G'_{\mathrm{TLM}} - \omega^2 L'_{\mathrm{TLM}} C'_{\mathrm{TLM}}\right)\end{array}}\,, \tag{9}$$

where R'_{TLM}, L'_{TLM}, C'_{TLM} and G'_{TLM} are defined by Fig. 3.

As damping is an exponential process, the voltage drop across the first few turns of the coil will be significantly larger when compared to the voltage drop over the following turns. The voltage drop across the first turn largely depends on the damping and the length of a single turn.

The capacitive path is electrically short and therefore allows for a fast propagation of high frequency components. For the concentrated winding, which is considered in this paper, it can be assumed that there is no significant capacitive coupling between the conductors of different phases.

In the following, the voltage drop between adjacent conductors of both machines is considered. For low frequencies, the topology of machine B yields an advantage over the topology of machine A as the first turn is only neighbouring with the second conductor. In machine A, the first conductor is also adjacent to conductor 47. The aim of this examination is to evaluate if this advantage for topology B is still existent at higher frequencies which occur in inverter-operated machines.

4. Measurement setup

In the following section, two measurement setups to estimate the propagation velocity and the damping constant are presented.

In order to estimate the propagation velocity, the stators of both exemplary machines are connected to a commercially available winding tester (*Schleich MTC 3*) as displayed in Fig. 6: Terminal u is connected to the stator tester, while the other ones are open. The housing is connected to the ground potential of the stator tester. The voltages U_1 (between terminal u and ground) and U_2 (between terminal v and ground) are measured between the ground connection and the power supply as well as the open terminal, respectively.

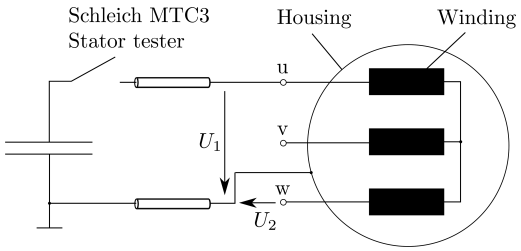

Fig. 6. Schematic of the setup to estimate the propagation velocity

The resulting voltages U_1 and U_2 for the stator with round wire winding are displayed in Fig. 7. It can be noticed that the most dominant frequency of the signal at the terminal u is significantly

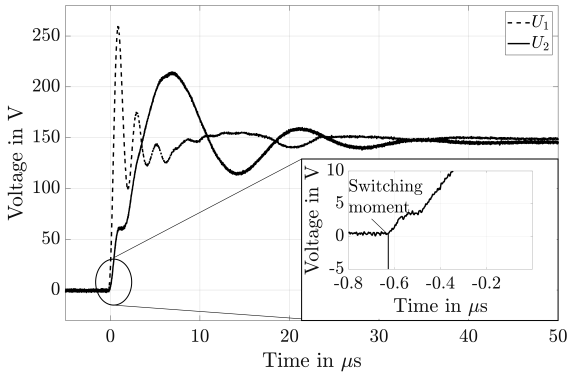

Fig. 7. Voltages U_1 and U_2 for the stator with round wire winding

damped when it reaches the open terminals v and w. Instead, a lower frequency component is pronounced. Regarding the timespan close to the switching process, it can be seen that the voltage U_2 rises immediately, even though the delay of a signal, which propagates at the vacuum speed of light along the winding, is 120 ns. This can be explained by the capacitive coupling between the turns, which allows for a significantly shorter path between the terminals for high frequency components. Signal U_2 is therefore composed of components that are conducted along the winding and components that are conducted via capacitive coupling. A direct measurement of the delay is therefore not possible.

The dominant frequency of the signal U_2 for machine A is located at 78.9 kHz while it is at 96.2 kHz for machine B. At these frequencies, both machines can still be considered as short when compared to the minimum wavelength (cp. Eq. (2)). Hence, the machine can be regarded as an L–C–R circuit where the eigenfrequency ω_e and the damping δ can be taken from the measurement (cp. Fig. 8). The resonant frequency ω_0 is given by:

$$\omega_0 = \sqrt{\omega_e^2 + \delta^2}\,. \tag{10}$$

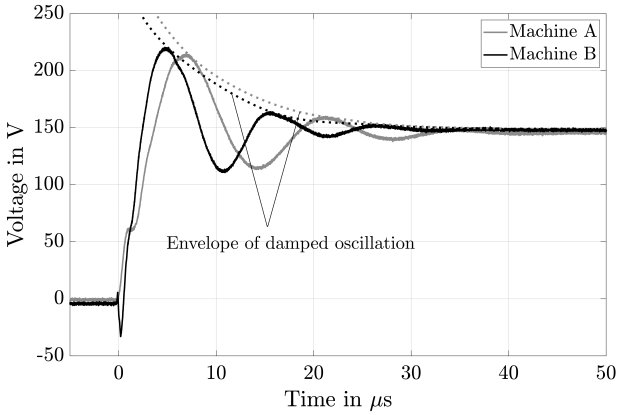

Fig. 8. Step response of machines A and B at terminal 2

The resonant frequency is merely depending on the capacitance C and the inductance L:

$$\omega_0 = \frac{1}{\sqrt{LC}}\,. \tag{11}$$

As long as the machine can be considered electrically short, the capacitance and inductance are calculated by multiplying the length of the winding l and the specific inductance L' and capacitance C', respectively. Therefore, the propagation velocity c can be calculated as:

$$c = \frac{1}{\sqrt{L'C'}} = l \cdot \omega_0\,. \tag{12}$$

The propagation velocities at the eigenfrequency for machines A and B are $c_\mathrm{A} = 18.5$ m/µs and $c_\mathrm{B} = 22.2$ m/µs, respectively. As stated above, SiC-inverters reach risetimes of 30 ns and less.

During this time span, a wave with the same propagation velocity would travel 0.56 m along the winding of machine A and 0.67 m along the winding of machine B, respectively. This corresponds to 3.1 turns for machine A and 3.7 turns for machine B. Due to its topology, this would result in a significant advantage for winding B. However, dispersion and capacitive coupling yield a significantly faster propagation of higher frequency components.

To assess the high frequency behaviour of the winding, the measurement setup is changed. For this work, a single coil of machine B is studied. The coil is positioned on a single stator tooth and placed inside an iron yoke (cp. Fig. 9). There is a solder contact on each turn in order to measure the voltage. The voltage between each turn and ground is measured. In order to achieve a sufficient amount of space inside the yoke while contacting the coil, one turn is removed. Therefore, 19 turns remain and the total length of the coil is reduced to $l_{\mathrm{coil}} = 3.42$ m.

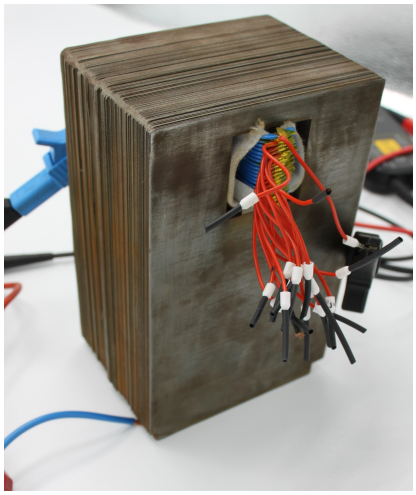

Fig. 9. Measurement setup of a single coil of machine B

The measured turn-to-ground voltage at the end of each turn is displayed in Fig. 10. From turn to turn, the time lag is increasing. The maximum voltage is decreasing from turn 1 to turn 13. Due to reflection at the open end of the setup, it is increasing from turn 13 to the open terminal at the end of the coil. In Fig. 11, the voltage wave forms of the input and the last turn are given. The rise time of the input signal is $t_{\mathrm{r}} = 27$ ns. The step therefore primarily excites a frequency of $f = 9.3$ MHz. The time lag between both signals is 45 ns. The resulting velocity of the voltage wave at this frequency is 76 m/µs and therefore significantly faster than at the eigenfrequency of the stator.

5. Analysis of the turn-to-turn voltage

To estimate the damping constant of the winding at 9.3 MHz, the voltage at the first five turns is evaluated. The reflection after turn 19 only has little influence in this region and is therefore not considered. In Fig. 12, the peak voltages of the terminal and the first five turns as well as the

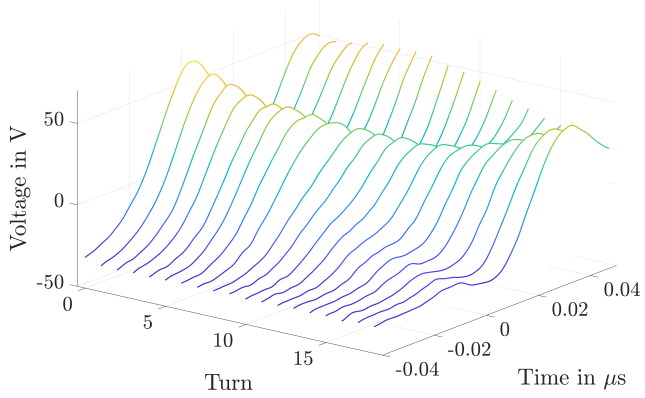

Fig. 10. Step response at each turn of one coil

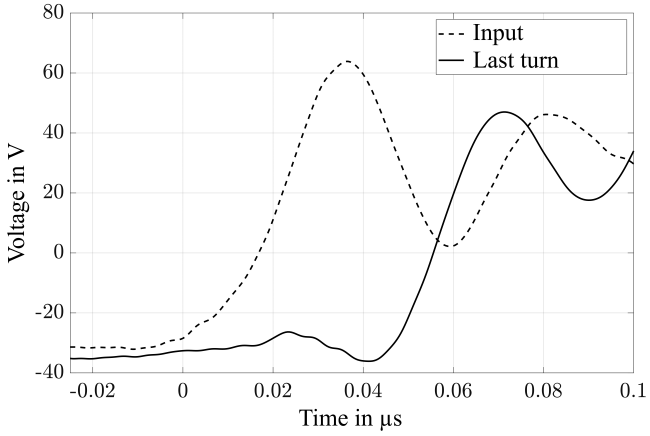

Fig. 11. Step response at the terminals of one coil

corresponding fitted exponential curve are displayed. The damping constant (cp Eq. (6)) can be estimated as $\alpha = 0.52\ \mathrm{m}^{-1}$.

Considering the coil geometry, the voltage wave travels 2.05 m or 11.4 turns during its risetime. Additionally, it is attenuated by 8.9% per turn. Combining both effects, it is expected that 16.9% of the peak voltage at the terminals will drop over the first turn.

A further increase of the voltage slew rate du/dt will lead to an increased voltage drop over the first few turns. Therefore, below a certain risetime, the advantage of winding topology B over winding topology A will be diminished. To further study this behaviour, the frequency dependency of the propagation constant γ and consequently on its real component α and imaginary part β (cp. Eqs. (7)–(9)) is examined. The capacitances of the coil are mostly frequency dependent as the permittivity of the insulation materials will decrease at high frequencies. The resistance and the inductance of the coils will change due to eddy effects. The current in the conductors will only flow close to the conductor surface at high frequencies. Consequently, the effective resistance will

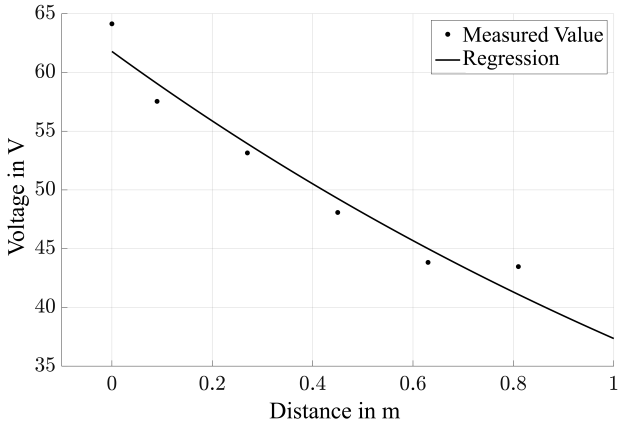

Fig. 12. Peak voltage as a function of distance to the input terminal

rise. At the same time, the inductance will be decreased as the magnetic field only penetrates the outer part of the yoke. For the winding topology of machine B, this behaviour is studied by using an FE-simulation.

For this purpose, a 2D model is used and the *Ansys Maxwell Eddy Current Field solver* is applied. The calculated inductances and resistances are displayed in Figs. 13 and 14. For the given machines, the loss factor of the insulation materials is in a range of 0.02 which indicates capacitive currents over the insulation are significantly more pronounced than conductive currents. The specific conductance G'_{TLM} in Eqs. (8) and (9) is therefore set to zero yielding the following equations:

$$\alpha = \sqrt{\frac{1}{2}\omega^2 L'_{\mathrm{TLM}} C'_{\mathrm{TLM}} \left(\sqrt{\frac{R'^2_{\mathrm{TLM}}}{\omega^2 L'^2_{\mathrm{TLM}}} + 1} - 1 \right)}, \tag{13}$$

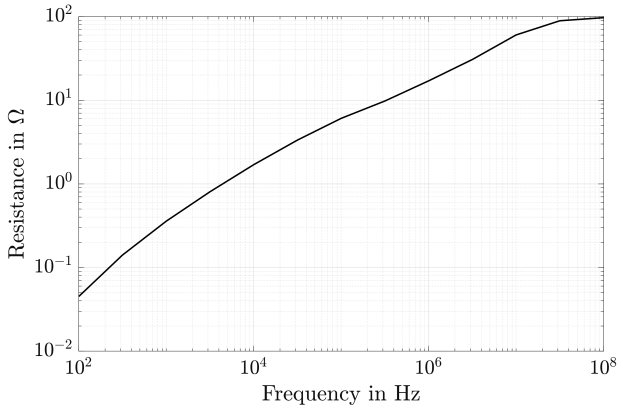

Fig. 13. Simulated resistance of the coil as a function of the frequency

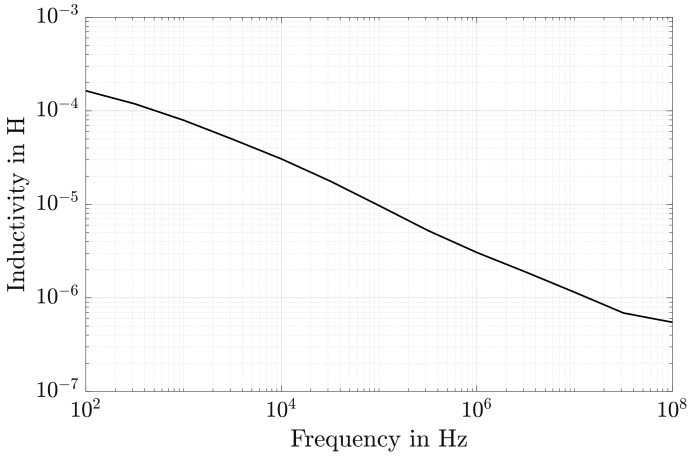

Fig. 14. Simulated inductivity of the coil as a function of the frequency

$$\beta = \sqrt{\frac{1}{2}\omega^2 L'_{\mathrm{TLM}} C'_{\mathrm{TLM}} \left(\sqrt{\frac{R'^2_{\mathrm{TLM}}}{\omega^2 L'^2_{\mathrm{TLM}}} + 1} + 1 \right)}. \tag{14}$$

By applying the damping factor of $\alpha = 1.68\ \mathrm{m}^{-1}$ and the calculated resistance and capacitance at 9.3 MHz, a specific capacitance of $C = 50$ nF/m is determined. To consider the frequency dependency of the damping factor, the frequency dependent resistances and inductances are inserted into Eq. (13). The damping factor as a function of frequency is displayed in Fig. 15.

In [19], the permittivity of epoxy is given for a frequency range of 1 MHz to 10 GHz.

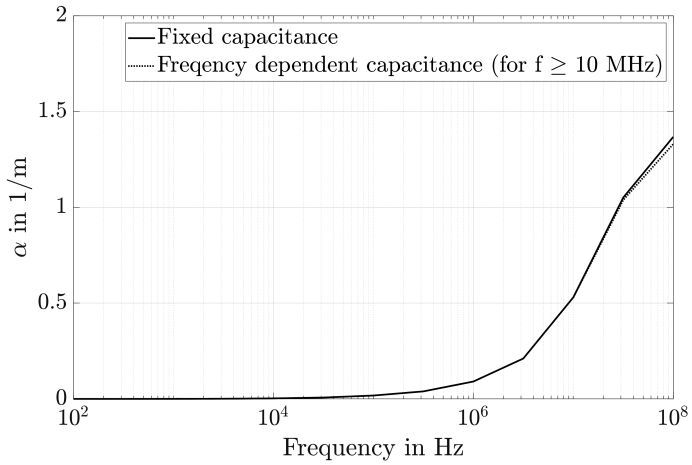

Fig. 15. Frequency dependent damping factor

Table 2. Relative permittivity of epoxy at various frequencies [19]

Frequency in MHz	**Rel. permittivity**
9.3	3.71
10	3.70
31	3.62
100	3.51

The datapoints, which are considered in this work, are given in Table 2. The considered winding is potted and it can be assumed that only a small fraction of the winding's volume consists of air enclosures. The relative capacitance C'_{TLM} is therefore assumed to be proportional to the relative permittivity ε_{r}:

$$C'_{\mathrm{TLM}} \propto \varepsilon_{\mathrm{r}} \,. \tag{15}$$

For frequencies of $f \geq 10$ MHz, the capacitance is adapted according to Eq. (15) and the data for the permittivity are collected in Table 2. The corresponding frequency dependent damping factor is added to the plot in Fig. 15. For the maximum frequency of 100 MHz, the relative error when neglecting the frequency dependence of the capacitance is 2.6%.

In Fig. 16, the frequency dependency of the propagation velocity is given. At a frequency of 100 MHz, which is considered being the maximum frequency in the scope of this paper, a propagation velocity of 93 m/µs is achieved. The timespan in which the voltage step needs to travel along the length of one turn is consequently $t_{\mathrm{turn}} = 1.9$ ns. The inverse of the damping constant α at this frequency equals 75 cm, the equivalent of 4.1 turns. At this location, the high frequency component of the voltage is damped by $(1 - \exp(-1)) = 63.2\%$. According to Eq. (4), a frequency of 100 MHz would be excited by a voltage with a risetime of $t_{\mathrm{r}} = 2.5$ ns. The voltage drop over the first turn of the winding is significantly smaller when compared to the peak voltage as long as

$$t_{\mathrm{r}} \gg t_{\mathrm{turn}} \tag{16}$$

and

$$\frac{1}{\alpha} \gg l_{\mathrm{turn}} \,. \tag{17}$$

Therefore, it can be assumed that the winding configuration of machine B still has an advantage over the conventional round wired winding of machine A. Applying state of the art SiC-inverters, only larger risetimes of $t_{\mathrm{r}} \gg 2.5$ ns are achieved. However, when applying GaN-semiconductors, a rise time in the same range of $t_{\mathrm{r}} = 4$ ns can be achieved [4]. From Eqs. (16) and (17) can be concluded that the portion of the voltage drop over the first turn converges to one as the size of the machine increases or the risetime decreases. For a slightly larger machine than considered in this paper the assumption, that the entire terminal voltage drops across the first turn, holds, when risetimes in the lower nanosecond range are applied.

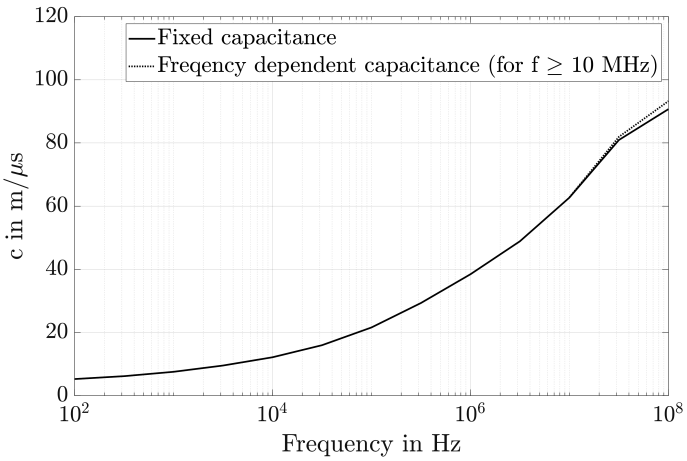

Fig. 16. Frequency dependent propagation velocity

6. Conclusions

In this paper, the transient behaviour of two machines with different winding topologies is studied. Machine A is equipped with a common round wire concentrated winding, while machine B is equipped with a preformed coil. Inside the preformed coil, only consecutive turns are physically placed next to each other. Following the general design rule, that the greatest part of the voltage drop occurs over just one turn, the interturn insulations of machines A and B would have to withstand the same voltage. To further study this phenomenon, the propagation velocity and damping of the transient voltage in both machines are studied by measuring the voltage at the output terminals of the stator. As the high frequency components of the voltage are completely mitigated at the output terminals, only the propagation velocity at the eigenfrequencies of machine c_A = 18.5 m/µs and machine B c_B = 22.2 m/µs can be obtained, indicating similar material properties of the insulation.

In machine A, turn 1 and turn 47 are adjacent to each other, leading to the conclusion that high frequency components are completely mitigated over such a long distance. Therefore, the coil of machine B is further considered. Measuring the voltage drop after each turn, the velocity of the transient with a rise time of t_r = 27 ns at its dominant frequency of 9.3 MHz is estimated to be 76 m/µs. Combined with a damping factor of α = 0.52 m^{-1} the portion of the voltage drop over the first turn is significantly smaller than one, yielding an advantage of winding topology B over topology A.

To consider higher frequencies, the damping factor and propagation velocity are estimated based on the results of an FE-Simulation. For the given size of the machine, it is estimated that the advantage of winding topology B over topology A completely vanishes at a risetime of $t_r < 1.9$ ns.

Acknowledgements

The specimens used in this paper are produced in the scope of the project "FlexiCoil" (funding number: 02P16A012), which is funded by the German Federal Ministry of Education and Research (BMBF) within the Framework Concept "Serienflexible Technologien für elektrische Antriebe von Fahrzeugen 2". The authors are grateful to the BMBF for the financing of this collaboration.

References

[1] Wright M.T., Yang S.J., McLeay K., *General theory of fast fronted interturn voltage distribution in electrical machine windings*, IEE Proceedings B (Electric Power Applications), vol. 130 no. 4, pp. 257–264 (1983), DOI: 10.1049/IP-B.1983.0040.

[2] McLaren P.G., Abdel-Rahman M.H., *Modeling of large AC motor coils for steep-fronted surge studies*, IEEE Transactions on Industry Applications, vol. 24, no. 3, pp. 422–426 (1988), DOI: 10.1109/28.2890.

[3] Toliyat H.A., Suresh G., Abur A., *Estimation of voltage distribution on the inverter fed random wound induction motor windings supplied through feeder cable*, IEEE Transactions on Energy Conversion, vol. 14, no. 4, pp. 976–981 (1999), DOI: 10.1109/60.815016.

[4] Wu Y.-F., Gritters J., Shen L., Smith R.P., Swenson B., *kV-Class GaN-on-Si HEMTs Enabling 99% Efficiency Converter at 800 V and 100 kHz*, IEEE Transactions on Power Electronics, vol. 29, no. 6, pp. 2634–2637 (2014), DOI: 10.1109/TPEL.2013.2284248.

[5] IEC 60034-18-41 ed. I, *Rotating electrical machines – Part 18–41: Partial discharge free electrical insulation systems (Type I) used in rotating electrical machines fed from voltage converters – Qualification and quality control tests* (2021).

[6] Magdun O., Blatt S., Binder A., *Calculation of stator winding parameters to predict the voltage distributions in inverter fed AC machines*, 2013 9th IEEE International Symposium on Diagnostics for Electric Machines, Power Electronics and Drives (SDEMPED), Valencia, Spain, pp. 447–453 (2013), DOI: 10.1109/DEMPED.2013.6645754.

[7] Ryu Y., Han K.J., *Improved transmission line model of the stator winding structure of an AC motor considering high-frequency conductor and dielectric effects,* 2017 IEEE International Electric Machines and Drives Conference (IEMDC), Miami, FL, USA, pp. 1–6 (2017), DOI: 10.1109/IEMDC.2017.8002140.

[8] Sousaferreira R., Ferreira A.C., *Analysis of End-Windings Influence on the Transient Voltage Distribution in Machine Stator Windings by a Three-Phase Model*, IEEE Transactions on Energy Conversion, vol. 36, no. 3 (2020), DOI: 10.1109/TEC.2020.3037453.

[9] Xie Y., Zhang J., Leonardi F., Munoz A.R., Liang F., Degner M.W., *Modeling and Verification of Electrical Stress in Inverter-Driven Electric Machine Windings*, 2018 IEEE Energy Conversion Congress and Exposition (ECCE), Portland, OR, USA, pp. 5742–5749 (2018), DOI: 10.1109/ECCE.2018.8558183.

[10] Pauli F., Driendl N., Hameyer K., *Study on Temperature Dependence of Partial Discharge in Low Voltage Traction Drives*, 2019 IEEE Workshop on Electrical Machines Design, Control and Diagnosis (WEMDCD), Athens, Greece, pp. 209–214 (2019), DOI: 10.1109/WEMDCD.2019.8887790.

[11] Lusuardi L., Cavallini A., de la Calle M.G., Martínez-Tarifa J.M., Robles G., *Insulation design of low voltage electrical motors fed by PWM inverters*, IEEE Electrical Insulation Magazine, vol. 35, no. 3, pp. 7–15 (2019), DOI: 10.1109/MEI.2019.8689431.

[12] Cavallini A., Fabiani D., Montanari G.C., *Power electronics and electrical insulation systems – part 2: life modeling for insulation design*, IEEE Electrical Insulation Magazine, vol. 26, no. 4, pp. 33–39 (2010), DOI: 10.1109/MEI.2010.5511187.

[13] Pauli F., Ruf A., Hameyer K., *Low voltage winding insulation systems under the influence of high du/dt slew rate inverter voltage*, Archives of Electrical Engineering, vol. 69, no. 1, pp. 187–202 (2020), DOI: 10.24425/aee.2020.131767.

[14] Pauli F., Groschup B., Schröder M., Hameyer K., *High Torque Density Low Voltage Traction Drives with Preformed Coils: Evaluation of Operating Limitations*, 2020 10th International Electric Drives Production Conference (EDPC), Ludwigsburg, Germany, pp. 1–8 (2020), DOI: 10.1109/EDPC51184.2020.9388214.

[15] Petrell D., Teller M., Hirt G., Börzel S. Schäfer W., *Economical production of conically shaped concentrated windings using forming technology for use in wheel hub engines*, 2020 10th International Electric Drives Production Conference (EDPC), Ludwigsburg, Germany, pp. 1–8 (2020), DOI: 10.1109/EDPC51184.2020.9388188.

[16] Pauli F., Schröder M., Hameyer K., *Design and Evaluation Methodology for Insulation Systems of Low Voltage Drives with Preformed Coils*, 2019 9th International Electric Drives Production Conference (EDPC), Esslingen, Germany, pp. 1–7 (2019), DOI: 10.1109/EDPC48408.2019.9012039.

[17] Küchler A., *High Voltage Engineering: Fundamentals – Technology – Applications*, Springer Vieweg, Berlin (2018).

[18] Mahdavi S., Hameyer K., *High frequency equivalent circuit model of the stator winding in electrical machines*, 2012 XXth International Conference on Electrical Machines, Marseille, France, pp. 1706–1711 (2012), DOI: 10.1109/ICElMach.2012.6350110.

[19] Singha S., Thomas M.J., *Permittivity and tan delta characteristics of epoxy nanocomposites in the frequency range of 1 MHz-1 GHz*, IEEE Transactions on Dielectrics and Electrical Insulation, vol. 15, no. 1, pp. 2–11 (2008), DOI: 10.1109/T-DEI.2008.4446731.